Yeast NDI1 expression prevents the unfolded protein response and reconfigures metabolism to restore neuronal function in mitochondrial complex I deficiency

Lucy Granat[1], Daniel Ranson[1], Emma Hamer[1], Ram Prosad Chakrabarty[2], Francesca Mattedi[1], Laura Fort-Aznar[3,4], Frank Hirth[1], Sean T. Sweeney[3], Alessio Vagnoni[1], Navdeep S. Chandel[2], Joseph M. Bateman[1]*

[1]Maurice Wohl Clinical Neuroscience Institute

King's College London

125 Coldharbour lane

London

SE5 9NU

UK

[2]Department of Medicine and Biochemistry & Molecular Genetics

Northwestern University Feinberg School of Medicine

Chicago

IL 60611

USA

[3]Department of Biology and York Biomedical Research Institute
University of York
Wentworth Way
Heslington
York, YO10 5DD
UK

4 Alzheimer's disease and other cognitive disorders Unit, Hospital Clínic de Barcelona

IDIBAPS, Universitat de Barcelona

Barcelona

08009

Spain

*Correspondence to: Joseph M. Bateman, joseph_matthew.bateman@kcl.ac.uk

Abstract

Mutations in mitochondrial complex I cause mitochondrial complex I deficiency, a group of severe neurological diseases that can result in death in infancy. The mechanisms underlying complex I deficiency pathogenesis remain poorly understood, and as a result there are currently no available treatments. To better understand the causes of neuronal dysfunction in complex I deficiency, we modelled complex I deficiency in *Drosophila* by knocking down the mitochondrial complex I subunit ND-75 (NDUFS1) specifically in neurons. Neuronal complex I deficiency causes locomotor defects, seizures and reduced lifespan. At the cellular level, complex I deficiency leads to mitochondrial morphology defects, reduced endoplasmic reticulum-mitochondria contacts and activation of the endoplasmic reticulum unfolded protein response (UPR) in neurons. Remarkably, we find that expression of the yeast non-proton translocating NADH dehydrogenase NDI1 in neurons, which couples NADH oxidation to transfer of electrons into the respiratory chain, reinstates endoplasmic reticulum-mitochondria contacts, prevents UPR activation and rescues the behavioural and lifespan phenotypes caused by complex I deficiency. Metabolomic analysis shows that NDI1 expression also reconfigures neuronal metabolism and implicates increased GABA levels as a contributor to the neurological manifestations of complex I deficiency. Together, these data indicate that NDI1 abrogates UPR signalling and reprogrammes metabolism to alleviate neuronal dysfunction caused by neuronal complex I deficiency.

Keywords

Mitochondria, ATF4, ROS, NADH/NAD+, signalling, neuron, NDUFS1

Introduction

Mitochondrial NADH dehydrogenase-ubiquinone oxidoreductase (complex I) is highly conserved: of the 44 unique subunits found in mammals 42 are present in Diptera (Agip et al., 2019; Garcia et al., 2017; Wirth et al., 2016). 14 complex I subunits are conserved in the prokaryotic NADH dehydrogenase-ubiquinone oxidoreductase, considered the core subunits essential for electron transport (Formosa et al., 2018). Knockout experiments have revealed that the accessory subunits present only in eukaryotes play important roles in complex I assembly and stability (Stroud et al., 2016). The majority of mitochondrial complex I subunits are encoded by the nuclear genome, while 7 of the core subunits are encoded by the mitochondrial genome (Formosa *et al.*, 2018). The subunits are grouped into 3 modules based on their location and role within the enzyme: the N module, which accepts electrons from NADH and forms the distal portion of the matrix arm, the Q module, which carries the electrons through iron-sulphur [Fe-S] clusters onto ubiquinone and forms the proximal portion of the matrix arm, and the P module, which contains the proton pumps and forms the membrane arm.

NAD+, generated by complex I activity through oxidation of NADH, is an essential coenzyme for tricarboxylic acid (TCA) enzymes isocitrate dehydrogenase, α-ketoglutarate dehydrogenase and malate dehydrogenase. Mitochondrial NAD+ also affects cytosolic NADH/NAD+ through the malate-aspartate and glycerol-3 phosphate shuttles (Spinelli and Haigis, 2018). NAD+ is important in a wide range of cellular processes and increasing NAD+/NADH is considered a potential therapy for a range of neurodegenerative and mitochondrial disease (Katsyuba et al., 2020).

The prevalence of primary mitochondrial diseases is predicted to be ~1 in 7634 at birth, and ~1 in 4300 by adulthood (Gorman et al., 2015; Skladal et al., 2003). Its high metabolic demand makes the CNS particularly susceptible to mitochondrial dysfunction, and neurological defects are the predominant symptoms of many mitochondrial diseases. Complex I deficiency is the most common childhood mitochondrial disease and is caused by mutations in genes encoding complex I structural or assembly components. Complex I deficiency encompasses a broad spectrum of disorders including Leigh syndrome, the most frequent and also one of the most severe (Fassone and Rahman, 2012). Leigh syndrome is a progressive neurological disorder characterised by severe psychomotor regression, alongside

the presence of symmetrical bilateral lesions within the brainstem and basal ganglia (Lake et al., 2016). Common neurological symptoms include seizures, dystonia, dysphagia, spasticity, developmental delay and optic atrophy (Finsterer, 2008; Sofou et al., 2014). Mutations in NDUF genes, including NDUFS1 and NDUFV1, are associated with particularly aggressive forms of Leigh syndrome causing death by four years of age (Lake *et al.*, 2016). However, there is considerable phenotypic heterogeneity in complex I deficiency, with examples of patients more mildly affected living to adulthood and with mild learning disability (Bjorkman et al., 2015; Koene et al., 2012).

There is also strong evidence to suggest that complex I deficiency contributes to pathogenesis in age-related neurodegenerative disease. Parkinson's disease (PD) is caused by loss of dopaminergic neurons in the *substantia nigra pars compacta* (SNc) and characterised by rigidity, tremors, bradykinesia and postural instability (Trinh and Farrer, 2013). Reduced complex I activity in the SNc is a neuropathological hallmark of PD (Schapira et al., 1989). Moreover, administration of complex I inhibitors, such as rotenone, cause dopaminergic neuron loss and PD-associated phenotypes in animal models and humans (Exner et al., 2012).

Perturbed mitochondrial function triggers mitochondrial stress signalling pathways. Mitochondrial stress signalling enables mitochondria to communicate with the nucleus and reprogram nuclear gene expression (Chandel, 2014; Granat et al., 2020; Hunt and Bateman, 2018). Mitochondrial stress signalling can act through different mechanisms, depending on the context. In higher eukaryotes, a common target of mitochondrial stress signalling is the activating transcription factor 4 (ATF4) (Hunt et al., 2019; Quiros et al., 2016; Quiros et al., 2017). ATF4 can be activated downstream of the endoplasmic reticulum unfolded protein response (UPR), or the integrated stress response (ISR). Importantly, targeting stress signalling pathways, including the UPR and ISR, has shown therapeutic potential in animal models.

Animal models of mitochondrial disease have provided valuable insights into disease mechanisms. Mouse and *Drosophila* complex I deficiency models have replicated many aspects of the human disease (Burman et al., 2014; Hegde et al., 2014; Kruse et al., 2008; Loewen and Ganetzky, 2018; McElroy et al., 2020; Quintana et al., 2010). However, previous models have not targeted neurons or investigated the role of mitochondrial stress signalling and the metabolic mechanisms underlying complex I deficiency. Here we experimentally interrogate a new neuron specific *Drosophila* model of mitochondrial complex I deficiency.

Knockdown of the core N module complex I subunit ND-75 (NDUFS1) in neurons causes neurological phenotypes including climbing and locomotor defects, seizures and greatly reduced lifespan. ND-75 knockdown in neurons perturbs mitochondrial morphology, causes reduced endoplasmic reticulum (ER)-mitochondria contacts and triggers the UPR, including activation of ATF4. Loss of ND-75 also alters cellular metabolism and perturbs the TCA cycle. Expression of the single subunit NADH dehydrogenase NDI1 in neurons rescues the aberrant mitochondrial morphology and loss of ER-mitochondria contacts resulting from ND-75 knockdown. UPR activation and ATF4 expression are also prevented by NDI1 expression. Remarkably, NDI1 almost completely rescues the severe behavioural and lifespan phenotypes caused by ND-75 knockdown. Metabolomic analysis shows that NDI1 expression reverses the changes in specific metabolites cause by ND-75 knockdown, including increased levels of the neurotransmitter GABA. These data provide novel insight into the mechanisms underlying the neurological manifestations of mitochondrial complex I deficiency in neurons.

Results

Knockdown of ND-75 in Drosophila neurons models mitochondrial complex I deficiency

Mutations in *NDUFS1* cause complex I deficiency and Leigh syndrome (Koene *et al.*, 2012; Lake *et al.*, 2016). Complex I forms the start of the electron transport chain, accepting electrons from NADH which then pass through the complex to ubiquinone. The subunits that form complex I are grouped into 3 modules: N, P and Q. NDUFS1 is an [Fe-S] cluster containing subunit involved in electron transfer which lies within the N model of the complex (Wirth *et al.*, 2016). To model complex I deficiency in *Drosophila* we used a previously validated short hairpin RNAi (HMS00853) targeting the *Drosophila* NDUFS1 homolog ND-75 (Toshniwal et al., 2019). We confirmed that ND-75 knockdown (hereafter referred to as ND-75^{KD}) ubiquitously in adult flies strongly reduced *ND-75* mRNA expression and caused an ~87% reduction in mitochondrial NADH dehydrogenase activity (Supplemental Fig. S1A, B). Ubiquitous ND-75^{KD} also significantly reduced the expression of ND-30 (Supplemental Fig. S1C-E), the orthologue of mammalian NDUFS3 and a component of Q module of complex I (Garcia *et al.*, 2017), suggesting collapse of the whole complex, and mirroring what has previously been observed with ND-75^{KD} in *Drosophila* muscle (Garcia *et al.*, 2017).

Motor impairments are frequently reported in complex deficiency patients (Finsterer, 2008). Pan-neuronal ND-75^{KD} using *nSyb-GAL4*, and with an independent non-overlapping short

hairpin RNAi (HMS00854), resulted in flies that were almost completely unable to climb (Fig. 1A, Supplemental Fig. S1F). To further analyse this locomotor phenotype we next measured open-field behaviour of ND-75^{KD} flies. The average speed and total distance moved by ND-75^{KD} flies was dramatically reduced, and immobility was increased compared to control flies (Fig. 1B-E). Together, these data demonstrate that ND-75^{KD} flies have severe motor dysfunction.

Alongside motor impairments, seizures are a common symptom of complex I deficiency (Finsterer and Zarrouk Mahjoub, 2012; Sofou *et al.*, 2014). Using a mechanical stress-induced seizure assay we found that ND-75^{KD} flies had a dramatic seizure phenotype, with 94% of flies developing seizures, which were significantly longer than controls and, in some cases, lasting four to five minutes (Fig. 1F, G). Together with severe neurological symptoms, complex I deficiency patients typically die within the first few years of life (Bjorkman *et al.*, 2015; Koene *et al.*, 2012). Consistent with this, ND-75^{KD} flies had dramatically reduced lifespan, with a median survival of five days, compared to 48 days for controls (Fig. 1H). Overall, these data show that neuronal-specific loss of ND-75 in *Drosophila* models the severe neurological manifestations of complex I deficiency.

ND-75^{KD} causes reduced neuronal ER-mitochondrial contacts

Mitochondria in fibroblasts isolated from patients with complex I deficiency have are fragmented and have significantly altered morphology (Koopman et al., 2007; Koopman et al., 2005). We therefore investigated the effect of complex I deficiency on mitochondrial morphology in neurons. Using super-resolution microscopy, we found that ND-75^{KD} in larval motor neurons led to striking alterations to the normal reticular mitochondrial morphology and a 76% increase in mitochondrial number (Fig. 2A-C). At the ultrastructural level, ND-75^{KD} did not obviously perturb mitochondrial cristae morphology in larval neurons or the adult brain (Fig. 2 G, H; Fig. 5K, M).

Changes to mitochondrial morphology lead to alterations in ER-mitochondria contacts (Cherubini et al., 2020; Cieri et al., 2018). Depending on the cell-type, it is estimated that ~5-35% of the mitochondrial network surface is in close proximity to the ER (McLelland et al., 2018; Rizzuto et al., 1998; Sood et al., 2014; Stoica et al., 2014). At sites of contact, mitochondria and the ER physically interact through the formation of tethering complexes (Csordás et al., 2006). (Csordás *et al.*, 2006). ER-mitochondria contacts play vital roles in

various processes including Ca^{2+} homeostasis, mitochondrial fission, autophagy and lipid transfer. In neurons, disturbance of these contacts is strongly associated with altered cellular signalling and disease (Celardo et al., 2016; Lee et al., 2018). Therefore, we next assessed whether ER-mitochondria contacts are affected in ND-75^{KD} neurons. To do this, we generated flies expressing the split-GFP-based contact site sensor (SPLICS) (Cieri *et al.*, 2018). SPLICS consists of an ER membrane-bound moiety and a mitochondrial membrane-bound moiety, which reconstitute to form a functional GFP protein when the ER and mitochondria are close enough (8-50 nm) to establish contacts. Mitochondrial morphological changes that alter ER-mitochondrial contacts are detected by SPLICS probes (Cherubini *et al.*, 2020; Cieri *et al.*, 2018). In neuronal cell bodies our SPLICS probe localised to puncta that were significantly reduced by knockdown of the ER-mitochondria tethering protein IP_3R (Lee et al., 2016), validating this tool (Supplemental Fig. S2A-C). ND-75^{KD} in larval motor neurons caused a significant reduction in the number of $SPLICS_L$ puncta (Fig. 2E-G), suggesting reduced ER-mitochondria connectivity. We confirmed this finding in the larval nervous system and adult brain at the ultrastructural level using transmission electron microscopy (Fig. 2H-J; Fig. 5U). These data suggest that the dramatic alteration in mitochondrial morphology resulting from ND-75 knockdown significantly reduces ER-mitochondria contacts.

PERK/ATF4 signalling is activated in ND-75^{KD} flies

Disruption of ER-mitochondria contacts has detrimental consequences for ER function, triggering ER stress and activation of the unfolded protein response (UPR), a stress signalling pathway (De Vos et al., 2012; Hetz and Mollereau, 2014). The unfolded protein response contributes to disease progression in multiple animal models of neurodegenerative disease (Hughes and Mallucci, 2019). To investigate whether the UPR is activated and acts as a mitochondrial stress signalling response in ND-75^{KD} flies, we analysed expression of the UPR transcription factor ATF4. ATF4 is not normally expressed in the nervous system but ND-75^{KD} caused strong activation of ATF4 expression in larval neurons and in the adult brain (Fig. 3A, C, E, F). Induction of the UPR activates protein kinase R-like endoplasmic reticulum kinase (PERK), resulting in ATF4 up-regulation through the phosphorylation of the translation initiation factor eIF2α (Hetz and Mollereau, 2014). Consistent with this, ND-75^{KD} increased phosphorylated eIF2α levels in neurons, and knockdown of PERK abrogated ATF4

activation (Fig. 3B, D, G-J). We therefore conclude that ATF4 is activated via the UPR and acts a mitochondrial stress signal in neurons with complex I deficiency.

To independently test the consequences of UPR activation in the nervous system we expressed dominant negative forms of the ER chaperone Hsc70-3 (GRP78, BiP), which ectopically activates the UPR (Elefant and Palter, 1999). Pan-neuronal expression of Hsc70-3^{D231S} with *nSyb-Gal4* caused pupal lethality, while expression of Hsc70-3^{K97S} caused a climbing defect (Supplemental Fig. 2D). This finding strongly suggests that activation of mitochondrial stress signalling and the UPR contributes to neuronal dysfunction in ND-75^{KD} knockdown flies.

Transcriptional and metabolic disruption in ND-75^{KD} flies

Our finding that the UPR is activated in ND-75^{KD} flies confirms that complex I deficiency triggers mitochondrial stress signalling in neurons, in keeping with previous in models of mitochondrial disease (Khan et al., 2017; Quiros *et al.*, 2017). To interrogate the transcriptional consequences of complex I deficiency in neurons we performed transcriptomic analysis of head tissue from ND-75^{KD} flies. The expression of 1694 genes were significantly increased, and 2017 genes significantly decreased in ND-75^{KD} flies (Supplemental Table S1), evidence of a strong mitochondrial stress induced transcriptional response. Gene ontology analysis (GEO) of cellular processes of genes with reduced expression ND-75^{KD} flies showed striking enrichment for mitochondrial genes (Fig. 4A). Kyoto encyclopaedia of genes and genomes (KEGG; (Ogata et al., 1999)) pathway analysis of genes with reduced expression ND-75^{KD} flies showed genes involved in oxidative phosphorylation and the TCA cycle as significantly enriched (Fig. 4B). Strikingly, in addition to ND-75, the expression of 28 genes encoding core or accessory subunits of complex I, or complex I assembly factors were significantly decreased in ND-75^{KD} flies, while none were significantly increased (Supplemental Tables S1, S2). Moreover, expression of multiple subunits of the other four mitochondrial respiratory complexes were significantly decreased in ND-75^{KD} flies (Supplemental Table S1). These data reveal a concerted transcriptional response to depress neuronal mitochondrial respiratory complex gene expression in ND-75^{KD} flies in response to complex I deficiency.

Genes encoding TCA cycle enzymes isocitrate dehydrogenase, succinyl-CoA synthetase, succinate dehydrogenase, fumarate hydratase, malate dehydrogenase, citrate synthase and components of the pyruvate dehydrogenase complex and oxoglutarate dehydrogenase complex were significantly decreased in ND-75^{KD} flies, whilst no TCA cycle genes were significantly increased (Supplemental Tables S1, S2), strongly implying that neuronal mitochondrial metabolism is perturbed in ND-75^{KD} flies. Following these striking observations, we performed metabolomic analysis of head tissue to directly analyse the mitochondrial metabolic changes in the brain caused by complex I deficiency. ND-75^{KD} flies had a significant increase in the level of 20 metabolites, and a significant decrease in the level of 25 metabolites compared to controls (Supplemental Table S3). Metabolite Set Enrichment Analysis (MSEA) showed significant dysregulation of several KEGG pathways in ND-75^{KD} fly heads (Fig. 4C). Consistent with inhibition of OXPHOS and increased aerobic glycolysis, pyruvate levels were significantly decreased in ND-75^{KD} flies (Supplemental Table S3). Moreover, levels of the TCA cycle intermediate fumarate were significantly decreased in ND-75^{KD} heads (Supplemental Table S3). 2-hydroxyglutarate levels were strongly increased (Supplemental Table S3), which we and others have shown is elevated in independent mitochondrial dysfunction/disease models (Burr et al., 2016; Hunt *et al.*, 2019). Glutamate and γ-aminobutyric acid (GABA) levels were also increased in ND-75^{KD} fly heads (Supplemental Table S3), indicating that neuronal complex I deficiency affects neurotransmitter levels. These observations further support the notion that complex I deficiency in neurons disrupts metabolism.

NADH oxidation by complex I replenishes NAD+, an essential coenzyme for the TCA cycle enzymes, while NADH inhibits regulatory TCA cycle enzymes. TCA cycle intermediates contribute to numerous other biosynthetic pathways, including amino acid, fatty acid and purine/pyrimidine synthesis (Lane and Fan, 2015; Spinelli and Haigis, 2018), suggesting that TCA cycle disruption within ND-75^{KD} flies will have wide ranging effects on neuronal function. We therefore hypothesised that impaired complex I NADH dehydrogenase activity is a key driver of neuronal dysfunction in ND-75^{KD} flies. To test this hypothesis we utilised the *Saccharomyces cerevisiae* single-subunit non-proton translocating NADH dehydrogenase NDI1, which oxidises mitochondrial NADH and transfers electrons to ubiquinone but does not directly contribute to ATP production (Seo et al., 1998). Metabolomic analysis of heads from flies with pan neuronal ND-75^{KD} combined with NDI1 expression showed a dramatically altered metabolite profile compared to ND-75^{KD} alone (Fig. 4D). Moreover, the

changes in the levels of pyruvate and fumarate caused by ND-75^{KD} were reversed by pan neuronal NDI1 expression (Fig. 4E, F). Interestingly, NDI1 expression also prevented the dramatic increase in GABA levels in ND-75^{KD} flies (Fig. 4G). Thus, expression of NDI1 reverses several of the key metabolic changes caused by knockdown of ND-75 in neurons.

NDI1 expression reinstates ER-mitochondria contacts, prevents UPR activation and rescues neuronal dysfunction and death caused by complex I deficiency

We next analysed the effects of NDI1 expression on the neuronal dysfunction caused by complex I deficiency. NDI1 expression dramatically improved the climbing defect and completely prevented seizures in ND-75^{KD} flies (Fig. 5A-C). Moreover, ND-75^{KD} flies expressing NDI1 had a median lifespan of 51 days, similar to controls (54 days; Fig. 5D).

Finally, following the observation that NDI1 expression rescues neuronal function in ND-75^{KD} neurons, we investigated whether NDI1 expression can ameliorate ND-75^{KD} induced changes to mitochondrial morphology, ER-mitochondria contacts and activation of the UPR. Strikingly, we found that NDI1 expression rescued the mitochondrial number and morphology changes (Fig. 6F-K), the loss of ER-mitochondria contacts (Fig. 6L-P) and prevented ATF4 activation caused by ND-75 knockdown (Fig. 6R-U).

Together, these data show that stress signalling activation, neuronal dysfunction and early death caused by complex I deficiency are rescued by the combined activities of NDI1 in *Drosophila*.

Discussion

Neurons are highly energetically and metabolically demanding and so are acutely sensitive to mitochondrial dysfunction. We have dissected the cellular and molecular mechanisms underlying neuronal complex I deficiency *in vivo* using ND-75^{KD} in *Drosophila*. Loss of complex I activity in neurons has profound effects on mitochondrial morphology and decreases ER-mitochondria contacts. ND-75^{KD} causes transcriptional reprogramming, potentially as an attempt to mitigate the loss of complex I activity, repressing complex I and TCA cycle gene expression. Consistent with this retrograde transcriptional response, we find activation of the ER UPR and expression of ATF4 in ND-75^{KD} neurons. Expression of NDI1

reverses key metabolic changes, restores normal mitochondrial morphology, prevents UPR activation and neuronal dysfunction in ND-75^{KD} flies.

Understanding the basis of the neurological manifestations of complex I deficiency in patients is hampered by the complex interactions between neurons and glia and the systemic effects of changes to tissues and organs outside the nervous system. Our ND-75^{KD} model provides cell autonomous insight into the effects of neuronal complex I deficiency *in vivo*. Neuronal ND-75^{KD} causes mitochondrial morphology changes, similar to those caused by knockout of the mitochondrial transcription factor TFAM in dopaminergic neurons (Sterky et al., 2011). The dramatic reduction in expression of respiratory and TCA cycle genes caused by ND-75^{KD} unbalances the expression of mitochondrial genes encoded by the nuclear and mitochondrial genomes. This disruption of inter-organelle gene expression may underly the mitochondrial morphology defects in ND-75^{KD} neurons. Interestingly, the master regulator of mitochondrial biogenesis PGC-1α is regulated by the NAD+-dependent deacetylase SIRT1 (Feige and Auwerx, 2007), providing a potential link between the loss of NADH dehydrogenase activity and mitochondrial biogenesis in ND-75^{KD} neurons.

Our data show that ND-75^{KD} activates ATF4 expression via the ER UPR in neurons. ER UPR activation likely contributes to the neurological defects in ND-75^{KD} flies as ectopic ER UPR activation via expression of dominant negative forms for Hsc70-3 also causes neuronal dysfunction. Activation of the ER UPR and integrated stress response (ISR) are frequently observed in response to mitochondrial dysfunction (Granat *et al.*, 2020; Hunt and Bateman, 2018; Quiros *et al.*, 2016). We have previously shown ER UPR and ATF4 activation due to mitochondrial dysfunction in *Drosophila* neurons using a TFAM overexpression model (Hunt *et al.*, 2019). Loss of Pink1, Parkin, DJ-1 or OXPHOS inhibition also cause ER UPR or ISR activation (Celardo *et al.*, 2016; Khan *et al.*, 2017; Quiros *et al.*, 2017; Yang et al., 2019). The direct cause of ER UPR and ISR activation in cells with dysfunctional mitochondria is much less well understood. Recently, screening approaches in cultured mammalian cells identified a novel OMA1-DELE1-HRI pathway that activates the ISR in response to mitochondrial dysfunction (Fessler et al., 2020; Guo et al., 2020). Whether this pathway is active in neurons is not known but *Drosophila* do not have an HRI kinase homolog, so this mechanism is unlikely to be relevant to stress signalling in *Drosophila*.

Modulation of mitochondrial morphology driven by Drp1 overexpression causes reduced ER-mitochondria contacts in mammalian cultured cells and primary neurons (Cherubini *et al.*,

2020; Cieri *et al.*, 2018). The reduced ER-mitochondria contacts in ND-75^{KD} neurons are therefore likely caused by the dramatic mitochondrial morphological changes. Increased mitochondrial fragmentation is seen in fibroblasts of complex I deficiency patients mutant for several complex I subunits, including NDUFS1 (Koopman *et al.*, 2007). ER-mitochondria tethering proteins are involved in regulation of the ER UPR, and modification of ER-mitochondria tethers can trigger UPR activation (Chu et al., 2019; Paillusson et al., 2016). Together with these studies, our data suggest that ER UPR activation is caused by reduced ER-mitochondrial contacts in ND-75^{KD} neurons. Altered ER-mitochondria contacts are a common feature of neurodegenerative disease and there is strong evidence to suggest that they play a pivotal role in disease pathogenesis (Paillusson *et al.*, 2016). Restoring ER-mitochondria contacts may therefore also have therapeutic potential in complex I deficiency.

NDI1 expression has been shown to extend lifespan and rescue the lethality caused by ubiquitous complex I deficiency in *Drosophila* (Bahadorani et al., 2010; Sanz et al., 2010). Viral expression of NDI1 into the *substantia nigra* protects against rotenone induced toxicity in a rat model of Parkinson's disease (Marella et al., 2008). In ageing models, NDI1 expression extends lifespan by increasing ROS through over reduction of the ubiquinone pool (Scialò et al., 2017). In the Ndufs4 knockout mouse model of Leigh syndrome, NDI1 expression rescues the lifespan but not motor defects, potentially through regenerating mitochondrial NAD+ from NADH (McElroy *et al.*, 2020). The in-depth knowledge of the mechanisms contributing to neuronal complex I deficiency afforded by the *Drosophila* ND-75^{KD} model may lead to therapeutic strategies tailored to combat the neurological manifestations in mitochondrial disease.

Acknowledgements

We are grateful to Rita Sousa-Nunes, Nazif Alic, Alex Whitworth and Darren Williams for fly stocks and the KCL Centre for Ultrastructural Imaging for technical assistance. Stocks obtained from the Bloomington *Drosophila* Stock Center (NIH P40OD018537) and the Vienna *Drosophila* Resource Center and FlyORF were used in this study. We are grateful to Ben Kottler for assistance with behavioural analyses, Sabrina Liu for help with climbing assays, Clare Steele-King of the York Imaging and Cytometry Facility for help with TEM, Peng Gao and the Robert H. Lurie Cancer Center Metabolomics Core at Northwestern University Feinberg School of Medicine for metabolomics analysis. We thank the Wohl

Cellular Imaging Centre at King's College London for help with light microscopy. This work was funded by Alzheimer's Research UK (ARUK-IRG2017A-2) and the MRC (MR/V013130/1) to JMB; LG was supported by the UK Medical Research Council (MR/N013700/1) and King's College London MRC Doctoral Training Partnership in Biomedical Sciences; STS and LFA were supported by a Motor Neurone Disease Association (UK) PhD studentship (Sweeney/Oct15/884-792) and a BBSRC project grant (BB/M002322/1) to STS; R.P.C was supported by a Northwestern University Pulmonary and Critical Care Department Cugell predoctoral fellowship.

Materials and Methods

Fly strains and growth conditions

Flies were maintained on standard yeast, glucose, cornmeal, agar food at 25^{o}C in a 12 hour light/dark cycle unless stated otherwise. Details of fly stocks are listed in Table S4. Fly stocks were obtained from the Bloomington Stock Center, the Vienna *Drosophila* Resource Center (Dietzl et al., 2007), the NIG-Fly Stock Center, Japan. For imaging experiments embryos were laid over a 24 hour period at 25^{o}C, incubated for a further 24 hours at 25^{o}C, then incubated at 29^{o}C for three days prior to analysis, unless stated otherwise.

Generation of SPLICS transgenic flies

To generate SPLICS flies, the $SPLICS_L$ insertions were sub-cloned from a pcDNA3 backbone (gift from Tito Calí; (Cieri et al., 2018)) into a pUASP vector as a BamHI-Xbal fragment. The pUASP-SPLICS construct was then integrated into the *Drosophila* genome by P-element mediated transposition. Embryo injections were performed by the Fly Facility of the Department of Genetics of the University of Cambridge.

Behavioural analysis

Climbing assays were performed as described previously (Hunt *et al.*, 2019).

For open-field locomotor activity flies were anaesthetised using CO_2 on the day of eclosion, and males of the desired genotype collected. Locomotor assays were performed the following morning, 1-4 hours after the start of the 12h light cycle. Flies were briefly anaesthetised on

ice and placed into individual open-field arenas 35mm in diameter and 1.8mm in height with vibrating motors attached (Kottler et al., 2019). Flies were left to acclimatise to the arenas for 15 minutes prior to the start of video recording. Flies were video recorded for a total of 2 hours 15 minutes: after an initial rest period of 30 minutes, flies were subjected to a mechanical stimulus (5 vibrations, 0.2 seconds long, 0.5 seconds apart) followed by 15 minutes recovery. This pattern of stimulus and recovery was repeated a further 5 times before a final rest period of 15 minutes. Tracking of individual flies and analysis of average speed, total distance and immobility was performed using Anymaze software (Stoelting).

Mechanical stress-induced seizure assays were performed using both male and female flies. Flies of the desired genotype were collected on the day of eclosion and added to fresh vials so that each vial contained a total of 2 flies. The following day, flies were transferred to an empty vial, and vortexed at full speed for 10 seconds. Immediately after vortexing, flies were observed for seizures. The 'bang-sensitive' seizure phenotype triggered by mechanical stress is well defined (Parker et al., 2011). A seizure was defined as a period of paralysis, potentially interspersed with limb twitching, wing movements and abdominal contractions. The length of each seizure was recorded, with the seizure considered to have ended when the fly stood upright.

Lifespan assays were performed using male flies. Male flies of the desired genotype were collected on the day of eclosion and added to fresh vials. 10 flies were initially added to each vial, and flies were incubated on their sides at 25°C for the duration of the assay. Every 2-3 days, flies were flipped into fresh vials and the number of dead flies in each vial were recorded. Dead flies that were carried over into the fresh vials were deducted from the next death count. Any flies that escaped during flipping, or were alive but stuck in the food so could not be flipped, were censored and deducted from the total fly count. Vials were flipped until all residing flies were dead.

qRT-PCR

qRT-PCR was performed as described previously (Hunt *et al.*, 2019). The following primers were used:

ND-75 forward: 5'-ACATTAACTACACGGGCAAGC-3'

ND-75 reverse: 5'- CAATCTCGGAGGCGAAAC-3'

Rpl4 forward: 5'-TCCACCTTGAAGAAGGGCTA-3'

Rpl4 reverse: 5'-TTGCGGATCTCCTCAGACTT-3'

Mitochondrial complex I assay

Flies were snap-frozen in liquid nitrogen and stored at -70°C until required. For each replicate, 30 females and 30 males were used. Flies were first ground together using a Potter-Elvehjem type homogeniser at 700rpm for 12 passes, in 600µl extraction buffer. The extraction buffer consisted of 250mM sucrose, 5mM Tris (pH 7.4), 2mM EGTA (pH 8.0) and 1% bovine serum albumin (BSA) in ddH2O. The resulting homogenates next underwent a series of centrifugation steps at 4°C. Firstly, samples were spun at 1000g for 5 minutes. Supernatants were then taken and again spun at 1000g for 5 minutes. Supernatants were taken again and spun at 3000g for 10 minutes. Supernatants were then discarded, and 5ml extraction buffer was added to the remaining pellets. After another round of centrifugation at 3000g for 10 minutes, the supernatants were again discarded, and 5ml extraction buffer containing sucrose, Tris and EGTA only (no BSA), was added to the pellets. Samples were then spun for a final time at 7000g for 10 minutes. Supernatants were removed and pellets (mitochondrial fraction) were resuspended in 500 µl of extraction buffer without BSA. The concentration of mitochondria in resuspended pellets was determined using a Pierce™ bicinchoninic acid (BCA) assay (Thermo Fisher Scientific) following the manufacturer's protocol.

Mitochondrial complex I and citrate synthase activity were assessed using a published protocol (Spinazzi et al., 2012). To disrupt mitochondrial membranes and maximise enzymatic readouts, isolated mitochondria underwent 3 freeze-thaw cycles prior to use.

For measurement of rotenone-sensitive complex I activity, 30µg/ml isolated mitochondria were added to a cuvette containing 100µl potassium phosphate buffer (0.5M, 0.5M potassium phosphate monobasic added to 0.5M potassium phosphate dibasic, pH 7.5), 60µl fatty acid-free BSA (50mg/ml), 30µl freshly prepared potassium cyanide (10mM) and 10µl freshly prepared NADH (10mM). A second, identical cuvette was prepared, with the addition of 10µl rotenone (1mM). Volumes were then adjusted to 994µl using ddH_2O. After mixing, baseline absorbance was read for 2 minutes at 340nm and 25°C using a SPECTROstar Nano (BMG Labtech). After recording of the baseline, 6µl ubiquinone1 (10 mM) was added to cuvettes, and the change in absorbance (Δabsorbance) was immediately recorded for 2 minutes at

340nm and 25°C. To calculate the ubiquinone-dependent Δabsorbance, the baseline Δabsorbance was subtracted from Δabsorbance recorded after ubiquinone1 addition. The rotenone-sensitive Δabsorbance for each sample was then calculated by subtracting the Δabsorbance/minute with rotenone from the Δabsorbance/minute without rotenone. Rotenone-sensitive complex I activity was calculated using the following equation: enzyme activity (nmol/min/mg) = (Δabsorbance/min × 1,000)/[(extinction coefficient × volume of sample used in ml) × (sample protein concentration in mg/ml)], where the extinction co-efficient = 6.2 (NADH), volume = 1 and sample protein concentration = 0.03.

For measurement of citrate synthase activity, 5µg/ml isolated mitochondria were added to a cuvette containing 500µl Tris (200mM, pH 8.0) with 0.2% Triton X-100, 100µl freshly prepared 5,5-dithio-bis-(2-nitrobenzoic acid) (DNTB, 1mM) and 30µl acetyl CoA (10 mM). Volumes were then adjusted to 950µl using ddH_2O. After mixing, baseline absorbance was read for 2 minutes at 412nm at 25°C using a SPECTROstar Nano (BMG Labtech). After recording of the baseline, 50µl freshly prepared oxaloacetic acid (10mM) was added to the sample, and the change in absorbance was recorded for 3 minutes at 412nm and 25°C. To calculate the oxaloacetic acid-dependent Δabsorbance, the baseline Δabsorbance was subtracted from Δabsorbance recorded after oxaloacetic acid addition. Citrate synthase activity was calculated using the same equation as for determining complex I activity, where the extinction co-efficient = 13.6 (TNB), volume = 1 and sample protein concentration = 0.005.

Immunofluorescence and imaging

Images were taken using a Nikon A1R confocal microscope or a Nikon Vt-iSIM super resolution microscope with NIS Elements software.

Antibody fluorescence levels were quantified using ImageJ. For experiments measuring larval ATF4 or eIF2α-P expression levels, the cellular membrane marker CD8-GFP was used to identify cells to be quantified. Maximum intensity projections were then produced from Z-stacks of the dorsal side of the VNC. For quantification of ATF4 levels, 20 nuclei were identified in the green channel (based off of CD8-GFP expression), and circled using the 'freehand selections' tool. The mean fluorescence intensity of the nuclei selected was then recorded in the ATF4 expression channel (red channel). The same method was used to quantify eIF2 α-P levels, except cytoplasmic regions were circled instead of nuclei. Primary

antibodies were rat anti-ATF4 (1:200, (Hunt *et al.*, 2019)), were rabbit anti-P-eIF2α (1:500, anti-Phospho-eIF2α [Ser51], Cell Signaling Technology 9721). Secondary antibodies were goat anti-rabbit Alexa Fluor 546 (Invitrogen A11035), goat anti-rat Alexa Fluor 555 (Thermo Fisher A21434).

The number of SPLICS GFP puncta was quantified using NIS-Elements advanced research software (v5.01.00, Nikon). Images of larval VNCs were first cropped in the XY plane so that only whole neuromeres remained. Next, images were processed using the 'General Analysis (GA3)' tool. Within GA3, an analysis flow chart was set up to identify and quantify the number of bright 3D spots within the GFP channel. The same diameter, z-axis elongation and intensity thresholds were applied to all images. The number of GFP spots in the image was used as a measure of the number of contacts per neuromere.

A Vt-iSIM super resolution microscope (Nikon) was used to capture mitoGFP expression. Samples were first located on the slide using 20x magnification. Images were taken at 100x magnification and 1.5x zoom using an SR Apo TIRF 100x oil immersion lens (NA=1.49). Z-stacks each 100nm in depth were taken of the dorsal side of the VNC. All Images taken were 1000 x 1440 pixels in size at a resolution of 43.29nm/pixel. Images were deconvolved within NIS-Elements software using a blind algorithm with 10 iterations. Images were analysed using Volocity (v6.3.1, PerkinElmer). A region of interest (ROI) 1.6x1.6µM in height and width was placed within a cell, positioned so that in all Z-stacks, the ROI remained within the same cell and excluded the nucleus. For each condition, a total of 30 ROIs were analysed from across 6 images, with each ROI placed in a different cell.

Western blot analysis

For each biological replicate, 10 male and 10 female flies were used. Flies were first homogenised in 40µl 1X sample buffer using a pestle in a 1.5ml Eppendorf and spun down at 14000g for 5 minutes. The 1X sample buffer consisted of 50mM Tris-HCl pH 6.8, 10% v/v glycerol, 2% w/v SDS and 0.01% w/v bromophenol blue. 100mM dithiothreitol (DTT) was added and samples were boiled at 95°C for 5 minutes. Samples were stored at -20°C. Antibodies were rabbit anti-VDAC (1:1000; ab14374, Abcam), mouse anti-Ndufs3 (1:500; ab14711, Abcam), rabbit anti-actin (1:5000; 4967, Cell Signalling Technology).

RNA sequencing (RNA-Seq) transcriptomic analysis

20 snap frozen fly heads (10 male and 10 female) were used for each replicate and placed into 100 µL of lysis buffer + β-mercaptoethanol from the Absolutely RNA Microprep kit (Agilent Technologies). Each genotype was prepared in quadruplicate. RNA was extracted from using the Absolutely RNA Microprep kit according to the manufacturer's protocol. The samples were sent on dry ice to Novogene Ltd. Sequencing libraries were generated using NEBNext® Ultra TM RNA Library Prep Kit for Illumina® (NEB, USA) following manufacturer's recommendations. The clustering of the index-coded samples was performed on a cBot Cluster Generation System using PE Cluster Kit cBot-HS (Illumina) according to the manufacturer's instructions. After cluster generation, the library preparations were sequenced on an Illumina platform and paired-end reads were generated. Raw data (raw reads) of FASTQ format were firstly processed through fastp. Paired-end clean reads were mapped to the *Drosophila*_melanogaster ensemble 102 genome using HISAT2 software. Featurecounts was used to count the read numbers mapped of each gene, then RPKM (Reads Per Kilobase of exon model per Million mapped reads) of each gene was calculated based on the length of the gene and reads count mapped to this gene (Trapnell et al., 2010). Differential expression analysis between conditions was performed using DESeq2 R package (Anders and Huber, 2010). P values were adjusted using the Benjamini and Hochberg's approach for controlling the False Discovery Rate (FDR). Genes with an adjusted P value < 0.05 found by DESeq2 were assigned as differentially expressed. GO enrichment analysis of differentially expressed genes was implemented by the clusterProfiler R package (Yu et al., 2012), in which gene length bias was corrected. GO terms with corrected P value less than 0.05 were considered significantly enriched by differential expressed genes. The clusterProfiler R package was used to test the statistical enrichment of differential expression genes in KEGG pathways.

Metabolomic analysis

20 snap frozen fly heads (10 male and 10 female) were used for each replicate. Untargeted metabolomic analysis was performed as in (Hunt et al., 2019). Metabolomic data were analysed using MetaboAnalyst 5.0 (Chong et al., 2018). Metabolites for which both conditions had fewer than 3 values > 0 were excluded from analysis. For pairwise global metabolite analysis, individual metabolite concentrations were compared using multiple unpaired two-way t-tests, and p values were adjusted for the FDR using the Benjamini–

Hochberg method for multiple-hypothesis testing (Benjamini and Hochberg, 1995). FDR-adjusted p values <0.05 were considered statistically significant. Pairwise MSEA was performed using the 'quantitative enrichment analysis (QEA)' algorithm (Xia and Wishart, 2010). The pathway-associated metabolite library (KEGG), containing 84 metabolite sets based on KEGG human metabolic pathways was used a reference library. Using QEA, a p value and a Q statistic, a description of the correlation between compound concentration profiles and clinical outcomes, were generated for each metabolic pathway. The actual Q-statistic calculated for each pathway was divided by the expected Q-statistic to provide the 'enrichment ratio'. FDR-adjusted p-values≤0.05 were considered statistically significant.

Transmission electron microscopy (TEM)

TEM of larval CNS tissue was performed as described previously (Cagin et al., 2015). Briefly, tissues from third instar wandering larvae were dissected and fixed in 0.1 M NaPO4, pH 7.4, 1% glutaraldehyde, and 4% formaldehyde, pH 7.3, overnight. Fixed larval preparations were washed 3× in 0.1 M $NaPO_4$ before incubation in OsO_4 (1% in 0.1 M $NaPO_4$, 1% potassium ferrocyanide (w/v) in 0.1 M $NaPO_4$; 2 h), dehydrated in an ethanol series, and embedded using Epon araldite resin. Sections were imaged using a transmission electron microscope (TECNAI 12 G2; FEI) with a camera (Soft Imaging Solutions MegaView; Olympus) and Tecnai user interface v2.1.8 and analySIS v3.2 (Soft Imaging Systems).

All dissected adult fly brain samples were post-fixed with 1% (w/v) osmium tetroxide and 1% potassium ferrocyanide (w/v) in 0.1M sodium phosphate buffer (pH 7.4) for 1 hour before being washed and dehydrated through a graded acetone series. Samples were then infiltrated with increasing concentrations of SPURR epoxy resin/acetone mixture before being placed into 100% resin overnight with rotation. The following day, the samples were infiltrated further before embedding (with the dorsal face orientated toward the sectioning plane) and polymerised at 70°C for 24 hours.

Ultrathin sections (50-70nm) were prepared using a Leica UC7 ultramicrotome (Leica microsystems, Vienna), mounted on grids and contrasted using UranyLess (22409 Electron Microscopy Sciences, USA) and lead citrate (22410 Electron Microscopy Sciences, USA). Samples were examined on a JEOL JEM 1400 Flash (JEOL, Japan) transmission microscope operated at 80 kV and images were acquired with a JEOL Flash Camera.

Mitochondrial contacts were quantified in ImageJ (version 1.52). Mitochondria with ER contacts were identified by observing a 30nm or less distance between the mitochondria and ER. For positive contacts, mitochondria circumferences were measured and recorded. The length of the ER with a distance <30nm was also measured and then divided by the mitochondria circumference to calculate the total length of the ER in contact.

Statistical analyses

Continuous data are expressed as mean ± S.E.M unless stated otherwise. Non-continuous data are expressed as percentages unless stated otherwise. Excluding metabolomic data, all data were analysed using Prism 8 (GraphPad). Student's unpaired two-way t-tests were used for pairwise comparisons of continuous data. An F-test was used to test for unequal variances, and where significant, Welch's correction was applied to the t-test. A one-way ANOVA with Tukey's post-hoc test was used for continuous data with multiple comparisons. Where variances were unequal, Welch's ANOVA followed by Dunnett's T3 multiple comparisons test was used. Chi-squared test and Fisher's tests were used for non-continuous data, and was applied to the raw values rather than percentages. The log-rank test was used for lifespan data. P values <0.05 were considered significant; * $p<0.05$, ** $p<0.01$, *** $p<0.001$, ****$p<0.0001$, n.s. non-significant. Experimental conditions where all values were equal to 0 were not included in statistical analysis.

References

Agip, A.A., Blaza, J.N., Fedor, J.G., and Hirst, J. (2019). Mammalian Respiratory Complex I Through the Lens of Cryo-EM. Annual review of biophysics *48*, 165-184. 10.1146/annurev-biophys-052118-115704.

Anders, S., and Huber, W. (2010). Differential expression analysis for sequence count data. Genome Biol *11*, R106. 10.1186/gb-2010-11-10-r106.

Bahadorani, S., Cho, J., Lo, T., Contreras, H., Lawal, H.O., Krantz, D.E., Bradley, T.J., and Walker, D.W. (2010). Neuronal expression of a single-subunit yeast NADH-ubiquinone oxidoreductase (Ndi1) extends Drosophila lifespan. Aging Cell *9*, 191-202. ACE546 [pii]

10.1111/j.1474-9726.2010.00546.x.

Benjamini, Y., and Hochberg, Y. (1995). Controlling the False Discovery Rate: A Practical and Powerful Approach to Multiple Testing. Journal of the Royal Statistical Society: Series B (Methodological) *57*, 289-300. https://doi.org/10.1111/j.2517-6161.1995.tb02031.x.

Bjorkman, K., Sofou, K., Darin, N., Holme, E., Kollberg, G., Asin-Cayuela, J., Holmberg Dahle, K.M., Oldfors, A., Moslemi, A.R., and Tulinius, M. (2015). Broad phenotypic variability in patients with complex I deficiency due to mutations in NDUFS1 and NDUFV1. Mitochondrion *21*, 33-40. 10.1016/j.mito.2015.01.003.

Burman, J.L., Itsara, L.S., Kayser, E.-B., Suthammarak, W., Wang, A.M., Kaeberlein, M., Sedensky, M.M., Morgan, P.G., and Pallanck, L.J. (2014). A Drosophila model of mitochondrial disease caused by a complex I mutation that uncouples proton pumping from electron transfer. Disease models & mechanisms *7*, 1165-1174. 10.1242/dmm.015321.

Burr, S.P., Costa, A.S., Grice, G.L., Timms, R.T., Lobb, I.T., Freisinger, P., Dodd, R.B., Dougan, G., Lehner, P.J., Frezza, C., and Nathan, J.A. (2016). Mitochondrial Protein Lipoylation and the 2-Oxoglutarate Dehydrogenase Complex Controls HIF1alpha Stability in Aerobic Conditions. Cell Metab *24*, 740-752. 10.1016/j.cmet.2016.09.015.

Cagin, U., Duncan, O.F., Gatt, A.P., Dionne, M.S., Sweeney, S.T., and Bateman, J.M. (2015). Mitochondrial retrograde signaling regulates neuronal function. Proc Natl Acad Sci U S A *112*, E6000-6009. 10.1073/pnas.1505036112.

Celardo, I., Costa, A.C., Lehmann, S., Jones, C., Wood, N., Mencacci, N.E., Mallucci, G.R., Loh, S.H., and Martins, L.M. (2016). Mitofusin-mediated ER stress triggers neurodegeneration in pink1/parkin models of Parkinson's disease. Cell Death Dis *7*, e2271. 10.1038/cddis.2016.173.

Chandel, N.S. (2014). Mitochondria as signaling organelles. BMC biology *12*, 34. 10.1186/1741-7007-12-34.

Cherubini, M., Lopez-Molina, L., and Gines, S. (2020). Mitochondrial fission in Huntington's disease mouse striatum disrupts ER-mitochondria contacts leading to disturbances in Ca(2+) efflux and Reactive Oxygen Species (ROS) homeostasis. Neurobiol Dis *136*, 104741. 10.1016/j.nbd.2020.104741.

Chong, J., Soufan, O., Li, C., Caraus, I., Li, S., Bourque, G., Wishart, D.S., and Xia, J. (2018). MetaboAnalyst 4.0: towards more transparent and integrative metabolomics analysis. Nucleic acids research *46*, W486-W494. 10.1093/nar/gky310.

Chu, Q., Martinez, T.F., Novak, S.W., Donaldson, C.J., Tan, D., Vaughan, J.M., Chang, T., Diedrich, J.K., Andrade, L., Kim, A., et al. (2019). Regulation of the ER stress response by a mitochondrial microprotein. Nature communications *10*, 4883. 10.1038/s41467-019-12816-z.

Cieri, D., Vicario, M., Giacomello, M., Vallese, F., Filadi, R., Wagner, T., Pozzan, T., Pizzo, P., Scorrano, L., Brini, M., and Calì, T. (2018). SPLICS: a split green fluorescent protein-

based contact site sensor for narrow and wide heterotypic organelle juxtaposition. Cell Death & Differentiation *25*, 1131-1145. 10.1038/s41418-017-0033-z.

Csordás, G., Renken, C., Várnai, P., Walter, L., Weaver, D., Buttle, K.F., Balla, T., Mannella, C.A., and Hajnóczky, G. (2006). Structural and functional features and significance of the physical linkage between ER and mitochondria. J Cell Biol *174*, 915-921. 10.1083/jcb.200604016.

De Vos, K.J., Mórotz, G.M., Stoica, R., Tudor, E.L., Lau, K.F., Ackerley, S., Warley, A., Shaw, C.E., and Miller, C.C. (2012). VAPB interacts with the mitochondrial protein PTPIP51 to regulate calcium homeostasis. Hum Mol Genet *21*, 1299-1311. 10.1093/hmg/ddr559.

Dietzl, G., Chen, D., Schnorrer, F., Su, K.C., Barinova, Y., Fellner, M., Gasser, B., Kinsey, K., Oppel, S., Scheiblauer, S., et al. (2007). A genome-wide transgenic RNAi library for conditional gene inactivation in Drosophila. Nature *448*, 151-156. nature05954 [pii]

10.1038/nature05954.

Elefant, F., and Palter, K.B. (1999). Tissue-specific expression of dominant negative mutant Drosophila HSC70 causes developmental defects and lethality. Mol Biol Cell *10*, 2101-2117. 10.1091/mbc.10.7.2101.

Exner, N., Lutz, A.K., Haass, C., and Winklhofer, K.F. (2012). Mitochondrial dysfunction in Parkinson's disease: molecular mechanisms and pathophysiological consequences. EMBO J *31*, 3038-3062. 10.1038/emboj.2012.170.

Fassone, E., and Rahman, S. (2012). Complex I deficiency: clinical features, biochemistry and molecular genetics. J Med Genet *49*, 578-590. 10.1136/jmedgenet-2012-101159.

Feige, J.N., and Auwerx, J. (2007). Transcriptional coregulators in the control of energy homeostasis. Trends Cell Biol *17*, 292-301. 10.1016/j.tcb.2007.04.001.

Fessler, E., Eckl, E.M., Schmitt, S., Mancilla, I.A., Meyer-Bender, M.F., Hanf, M., Philippou-Massier, J., Krebs, S., Zischka, H., and Jae, L.T. (2020). A pathway coordinated by DELE1 relays mitochondrial stress to the cytosol. Nature *579*, 433-437. 10.1038/s41586-020-2076-4.

Finsterer, J. (2008). Leigh and Leigh-Like Syndrome in Children and Adults. Pediatric neurology *39*, 223-235. https://doi.org/10.1016/j.pediatrneurol.2008.07.013.

Finsterer, J., and Zarrouk Mahjoub, S. (2012). Epilepsy in mitochondrial disorders. Seizure *21*, 316-321. 10.1016/j.seizure.2012.03.003.

Formosa, L.E., Dibley, M.G., Stroud, D.A., and Ryan, M.T. (2018). Building a complex complex: Assembly of mitochondrial respiratory chain complex I. Seminars in Cell & Developmental Biology *76*, 154-162. https://doi.org/10.1016/j.semcdb.2017.08.011.

Garcia, C.J., Khajeh, J., Coulanges, E., Chen, E.I.J., and Owusu-Ansah, E. (2017). Regulation of Mitochondrial Complex I Biogenesis in Drosophila Flight Muscles. Cell reports *20*, 264-278. 10.1016/j.celrep.2017.06.015.

Gorman, G.S., Schaefer, A.M., Ng, Y., Gomez, N., Blakely, E.L., Alston, C.L., Feeney, C., Horvath, R., Yu-Wai-Man, P., Chinnery, P.F., et al. (2015). Prevalence of nuclear and mitochondrial DNA mutations related to adult mitochondrial disease. Annals of neurology *77*, 753-759. 10.1002/ana.24362.

Granat, L., Hunt, R.J., and Bateman, J.M. (2020). Mitochondrial retrograde signalling in neurological disease. Philos Trans R Soc Lond B Biol Sci *375*, 20190415. 10.1098/rstb.2019.0415.

Guo, X., Aviles, G., Liu, Y., Tian, R., Unger, B.A., Lin, Y.T., Wiita, A.P., Xu, K., Correia, M.A., and Kampmann, M. (2020). Mitochondrial stress is relayed to the cytosol by an OMA1-DELE1-HRI pathway. Nature *579*, 427-432. 10.1038/s41586-020-2078-2.

Hegde, V.R., Vogel, R., and Feany, M.B. (2014). Glia are critical for the neuropathology of complex I deficiency in Drosophila. Hum Mol Genet *23*, 4686-4692. 10.1093/hmg/ddu188.

Hetz, C., and Mollereau, B. (2014). Disturbance of endoplasmic reticulum proteostasis in neurodegenerative diseases. Nature reviews. Neuroscience *15*, 233-249. 10.1038/nrn3689.

Hughes, D., and Mallucci, G.R. (2019). The unfolded protein response in neurodegenerative disorders - therapeutic modulation of the PERK pathway. The FEBS journal *286*, 342-355. 10.1111/febs.14422.

Hunt, R.J., and Bateman, J.M. (2018). Mitochondrial retrograde signaling in the nervous system. FEBS Lett *592*, 663-678. 10.1002/1873-3468.12890.

Hunt, R.J., Granat, L., McElroy, G.S., Ranganathan, R., Chandel, N.S., and Bateman, J.M. (2019). Mitochondrial stress causes neuronal dysfunction via an ATF4-dependent increase in L-2-hydroxyglutarate. J Cell Biol *218*, 4007-4016. 10.1083/jcb.201904148.

Katsyuba, E., Romani, M., Hofer, D., and Auwerx, J. (2020). NAD(+) homeostasis in health and disease. Nature metabolism *2*, 9-31. 10.1038/s42255-019-0161-5.

Khan, N.A., Nikkanen, J., Yatsuga, S., Jackson, C., Wang, L., Pradhan, S., Kivela, R., Pessia, A., Velagapudi, V., and Suomalainen, A. (2017). mTORC1 Regulates Mitochondrial Integrated Stress Response and Mitochondrial Myopathy Progression. Cell Metab *26*, 419-428.e415. 10.1016/j.cmet.2017.07.007.

Koene, S., Rodenburg, R.J., van der Knaap, M.S., Willemsen, M.A.A.P., Sperl, W., Laugel, V., Ostergaard, E., Tarnopolsky, M., Martin, M.A., Nesbitt, V., et al. (2012). Natural disease course and genotype-phenotype correlations in Complex I deficiency caused by nuclear gene defects: what we learned from 130 cases. Journal of inherited metabolic disease *35*, 737-747. 10.1007/s10545-012-9492-z.

Koopman, W.J., Verkaart, S., Visch, H.J., van Emst-de Vries, S., Nijtmans, L.G., Smeitink, J.A., and Willems, P.H. (2007). Human NADH:ubiquinone oxidoreductase deficiency: radical changes in mitochondrial morphology? American journal of physiology. Cell physiology *293*, C22-29. 10.1152/ajpcell.00194.2006.

Koopman, W.J., Visch, H.J., Verkaart, S., van den Heuvel, L.W., Smeitink, J.A., and Willems, P.H. (2005). Mitochondrial network complexity and pathological decrease in complex I activity are tightly correlated in isolated human complex I deficiency. American journal of physiology. Cell physiology *289*, C881-890. 10.1152/ajpcell.00104.2005.

Kottler, B., Faville, R., Bridi, J.C., and Hirth, F. (2019). Inverse Control of Turning Behavior by Dopamine D1 Receptor Signaling in Columnar and Ring Neurons of the Central Complex in Drosophila. Curr Biol *29*, 567-577.e566. 10.1016/j.cub.2019.01.017.

Kruse, S.E., Watt, W.C., Marcinek, D.J., Kapur, R.P., Schenkman, K.A., and Palmiter, R.D. (2008). Mice with mitochondrial complex I deficiency develop a fatal encephalomyopathy. Cell Metab *7*, 312-320. 10.1016/j.cmet.2008.02.004.

Lake, N.J., Compton, A.G., Rahman, S., and Thorburn, D.R. (2016). Leigh syndrome: One disorder, more than 75 monogenic causes. Annals of neurology *79*, 190-203. 10.1002/ana.24551.

Lane, A.N., and Fan, T.W.M. (2015). Regulation of mammalian nucleotide metabolism and biosynthesis. Nucleic acids research *43*, 2466-2485. 10.1093/nar/gkv047.

Lee, K.S., Huh, S., Lee, S., Wu, Z., Kim, A.K., Kang, H.Y., and Lu, B. (2018). Altered ER-mitochondria contact impacts mitochondria calcium homeostasis and contributes to neurodegeneration in vivo in disease models. Proc Natl Acad Sci U S A *115*, E8844-e8853. 10.1073/pnas.1721136115.

Lee, S., Lee, K.-S., Huh, S., Liu, S., Lee, D.-Y., Hong, Seung H., Yu, K., and Lu, B. (2016). Polo Kinase Phosphorylates Miro to Control ER-Mitochondria Contact Sites and Mitochondrial Ca2+ Homeostasis in Neural Stem Cell Development. Developmental Cell *37*, 174-189. 10.1016/j.devcel.2016.03.023.

Loewen, C.A., and Ganetzky, B. (2018). Mito-Nuclear Interactions Affecting Lifespan and Neurodegeneration in a Drosophila Model of Leigh Syndrome. Genetics *208*, 1535-1552. 10.1534/genetics.118.300818.

Marella, M., Seo, B.B., Nakamaru-Ogiso, E., Greenamyre, J.T., Matsuno-Yagi, A., and Yagi, T. (2008). Protection by the NDI1 gene against neurodegeneration in a rotenone rat model of Parkinson's disease. PloS one *3*, e1433. 10.1371/journal.pone.0001433.

McElroy, G.S., Reczek, C.R., Reyfman, P.A., Mithal, D.S., Horbinski, C.M., and Chandel, N.S. (2020). NAD+ Regeneration Rescues Lifespan, but Not Ataxia, in a Mouse Model of Brain Mitochondrial Complex I Dysfunction. Cell Metab *32*, 301-308.e306. 10.1016/j.cmet.2020.06.003.

Ogata, H., Goto, S., Sato, K., Fujibuchi, W., Bono, H., and Kanehisa, M. (1999). KEGG: Kyoto Encyclopedia of Genes and Genomes. Nucleic Acids Res *27*, 29-34. 10.1093/nar/27.1.29.

Paillusson, S., Stoica, R., Gomez-Suaga, P., Lau, D.H., Mueller, S., Miller, T., and Miller, C.C. (2016). There's Something Wrong with my MAM; the ER-Mitochondria Axis and Neurodegenerative Diseases. Trends Neurosci *39*, 146-157. 10.1016/j.tins.2016.01.008.

Parker, L., Howlett, I.C., Rusan, Z.M., and Tanouye, M.A. (2011). Seizure and epilepsy: studies of seizure disorders in Drosophila. International review of neurobiology *99*, 1-21. 10.1016/b978-0-12-387003-2.00001-x.

Quintana, A., Kruse, S.E., Kapur, R.P., Sanz, E., and Palmiter, R.D. (2010). Complex I deficiency due to loss of Ndufs4 in the brain results in progressive encephalopathy resembling Leigh syndrome. Proc Natl Acad Sci U S A *107*, 10996-11001. 10.1073/pnas.1006214107.

Quiros, P.M., Mottis, A., and Auwerx, J. (2016). Mitonuclear communication in homeostasis and stress. Nature reviews. Molecular cell biology *17*, 213-226. 10.1038/nrm.2016.23.

Quiros, P.M., Prado, M.A., Zamboni, N., D'Amico, D., Williams, R.W., Finley, D., Gygi, S.P., and Auwerx, J. (2017). Multi-omics analysis identifies ATF4 as a key regulator of the mitochondrial stress response in mammals. J Cell Biol *216*, 2027-2045. 10.1083/jcb.201702058.

Sanz, A., Soikkeli, M., Portero-Otin, M., Wilson, A., Kemppainen, E., McIlroy, G., Ellila, S., Kemppainen, K.K., Tuomela, T., Lakanmaa, M., et al. (2010). Expression of the yeast NADH dehydrogenase Ndi1 in Drosophila confers increased lifespan independently of dietary restriction. Proc Natl Acad Sci U S A *107*, 9105-9110. 0911539107 [pii]

10.1073/pnas.0911539107.

Schapira, A.H., Cooper, J.M., Dexter, D., Jenner, P., Clark, J.B., and Marsden, C.D. (1989). Mitochondrial complex I deficiency in Parkinson's disease. Lancet *1*, 1269. S0140-6736(89)92366-0 [pii].

Scialò, F., Fernández-Ayala, D.J., and Sanz, A. (2017). Role of Mitochondrial Reverse Electron Transport in ROS Signaling: Potential Roles in Health and Disease. Frontiers in physiology *8*, 428-428. 10.3389/fphys.2017.00428.

Seo, B.B., Kitajima-Ihara, T., Chan, E.K., Scheffler, I.E., Matsuno-Yagi, A., and Yagi, T. (1998). Molecular remedy of complex I defects: rotenone-insensitive internal NADH-quinone oxidoreductase of Saccharomyces cerevisiae mitochondria restores the NADH oxidase activity of complex I-deficient mammalian cells. Proc Natl Acad Sci U S A *95*, 9167-9171. 10.1073/pnas.95.16.9167.

Skladal, D., Halliday, J., and Thorburn, D.R. (2003). Minimum birth prevalence of mitochondrial respiratory chain disorders in children. Brain *126*, 1905-1912. 10.1093/brain/awg170.

Sofou, K., De Coo, I.F., Isohanni, P., Ostergaard, E., Naess, K., De Meirleir, L., Tzoulis, C., Uusimaa, J., De Angst, I.B., Lönnqvist, T., et al. (2014). A multicenter study on Leigh syndrome: disease course and predictors of survival. Orphanet journal of rare diseases *9*, 52. 10.1186/1750-1172-9-52.

Spinazzi, M., Casarin, A., Pertegato, V., Salviati, L., and Angelini, C. (2012). Assessment of mitochondrial respiratory chain enzymatic activities on tissues and cultured cells. Nature Protocols *7*, 1235-1246. 10.1038/nprot.2012.058.

Spinelli, J.B., and Haigis, M.C. (2018). The multifaceted contributions of mitochondria to cellular metabolism. Nat Cell Biol *20*, 745-754. 10.1038/s41556-018-0124-1.

Sterky, F.H., Lee, S., Wibom, R., Olson, L., and Larsson, N.G. (2011). Impaired mitochondrial transport and Parkin-independent degeneration of respiratory chain-deficient dopamine neurons in vivo. Proc Natl Acad Sci U S A *108*, 12937-12942. 1103295108 [pii]

10.1073/pnas.1103295108.

Stroud, D.A., Surgenor, E.E., Formosa, L.E., Reljic, B., Frazier, A.E., Dibley, M.G., Osellame, L.D., Stait, T., Beilharz, T.H., Thorburn, D.R., et al. (2016). Accessory subunits are integral for assembly and function of human mitochondrial complex I. Nature *538*, 123-126. 10.1038/nature19754.

Toshniwal, A.G., Gupta, S., Mandal, L., and Mandal, S. (2019). ROS Inhibits Cell Growth by Regulating 4EBP and S6K, Independent of TOR, during Development. Dev Cell *49*, 473-489.e479. 10.1016/j.devcel.2019.04.008.

Trapnell, C., Williams, B.A., Pertea, G., Mortazavi, A., Kwan, G., van Baren, M.J., Salzberg, S.L., Wold, B.J., and Pachter, L. (2010). Transcript assembly and quantification by RNA-Seq reveals unannotated transcripts and isoform switching during cell differentiation. Nature biotechnology *28*, 511-515. 10.1038/nbt.1621.

Trinh, J., and Farrer, M. (2013). Advances in the genetics of Parkinson disease. Nat Rev Neurol *9*, 445-454. 10.1038/nrneurol.2013.132.

Wirth, C., Brandt, U., Hunte, C., and Zickermann, V. (2016). Structure and function of mitochondrial complex I. Biochimica et Biophysica Acta (BBA) - Bioenergetics *1857*, 902-914. https://doi.org/10.1016/j.bbabio.2016.02.013.

Xia, J., and Wishart, D.S. (2010). MSEA: a web-based tool to identify biologically meaningful patterns in quantitative metabolomic data. Nucleic Acids Res *38*, W71-77. 10.1093/nar/gkq329.

Yang, J., Kim, K.S., Iyirhiaro, G.O., Marcogliese, P.C., Callaghan, S.M., Qu, D., Kim, W.J., Slack, R.S., and Park, D.S. (2019). DJ-1 modulates the unfolded protein response and cell death via upregulation of ATF4 following ER stress. Cell Death Dis *10*, 135. 10.1038/s41419-019-1354-2.

Yu, G., Wang, L.G., Han, Y., and He, Q.Y. (2012). clusterProfiler: an R package for comparing biological themes among gene clusters. Omics : a journal of integrative biology *16*, 284-287. 10.1089/omi.2011.0118.

Figures

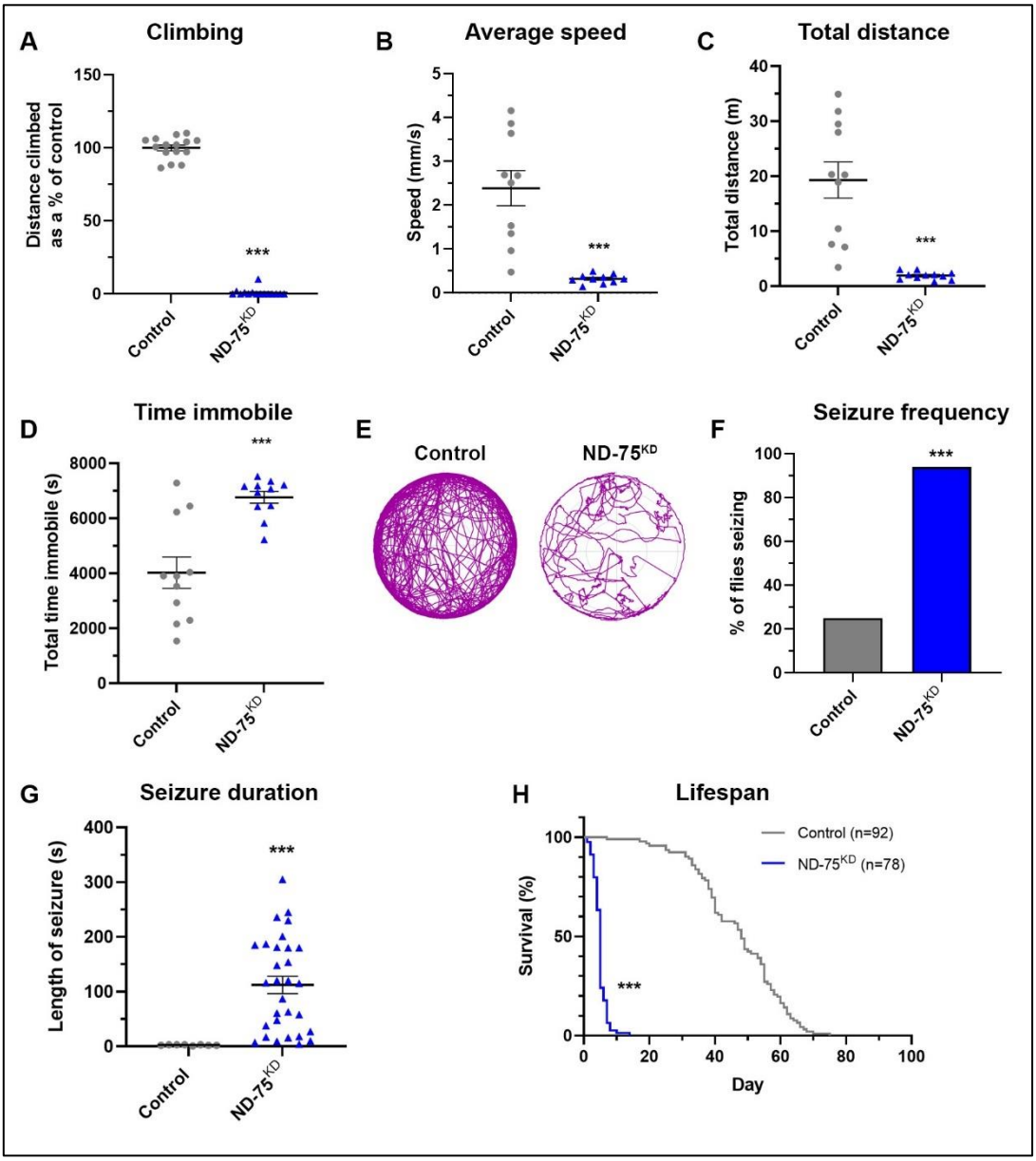

Figure 1. ND-75^{KD} flies have reduced mobility, seizures and decreased lifespan. (A) ND-75^{KD} flies are almost completely unable to climb. (B-D) In an 135 min open field assay, ND-75^{KD} flies have reduced average speed (B), move a shorter total distance (C) and spend more

time immobile (D). (E) Example open field track plot of control and ND-75^{KD} flies. (F, G) ND-75^{KD} flies have more seizures than controls (F), which last up 4-5 mins in some cases (G). (H) Lifespan is greatly reduced in ND-75^{KD} flies. ND-75 RNAi expressed using *Tub-Gal80^{ts}*; *nSyb-Gal4*. Controls are *Tub-Gal80^{ts}*; *nSyb-Gal4* hemizygotes. Data are represented as mean ± SEM. Student's t test, Chi-squared for seizure frequency, or log-rank test for survival curve. *p<0.05, ***p < 0.001.

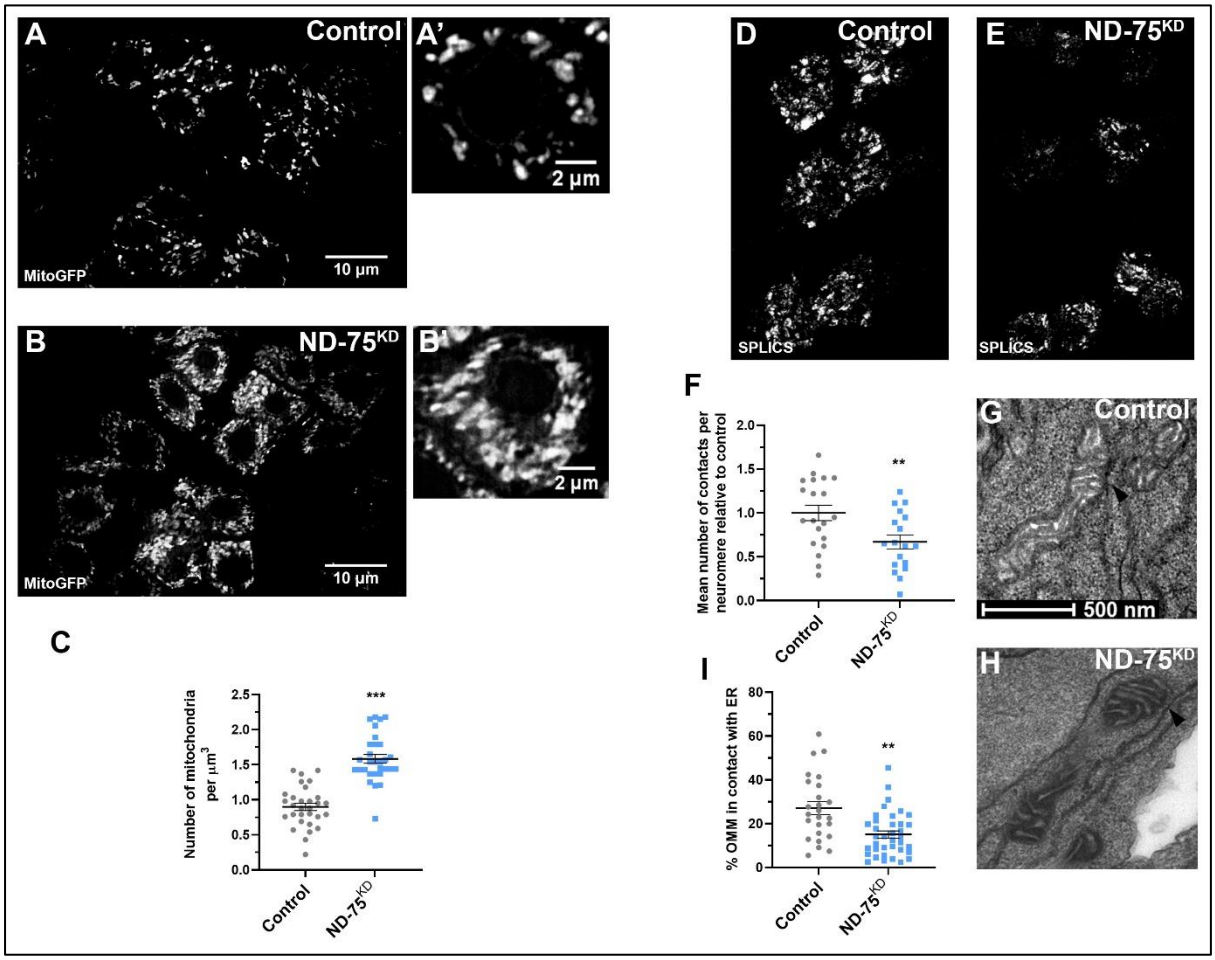

Figure 2. ND-75^{KD} in neurons causes aberrant mitochondrial morphology and reduced ER-mitochondria contacts. (A, B) Expression of mitochondria-targeted GFP (mitoGFP) to visualise mitochondria in control (A) or ND-75 knockdown (B) larval motor neurons using *OK371-Gal4*. Imaged using iSIM. (C, D) Quantification of mitochondrial number (C) in larval motor neurons with ND-75 knockdown using *OK371-Gal4*. (D, E) Visualisation of ER-mitochondria contacts by split-GFP-based contact site sensor (SPLICS) expression in control (D) or ND-75 knockdown (E) larval motor neurons using *OK371-Gal4*. (F) Quantification of SPLICS puncta. (G, H) Transmission electron microscopy images of mitochondria in larval CNS tissue from control or with pan-neuronal ND-75 knockdown (using *nSyb-Gal4*). Arrowheads indicate ER-mitochondria contacts. (I) Quantification of ER-mitochondria contacts. Controls are *OK371-Gal4* or *nSyb-Gal4* hemizygotes. Data are represented as mean ± SEM. Student's t test. **p<0.01, ***p < 0.001.

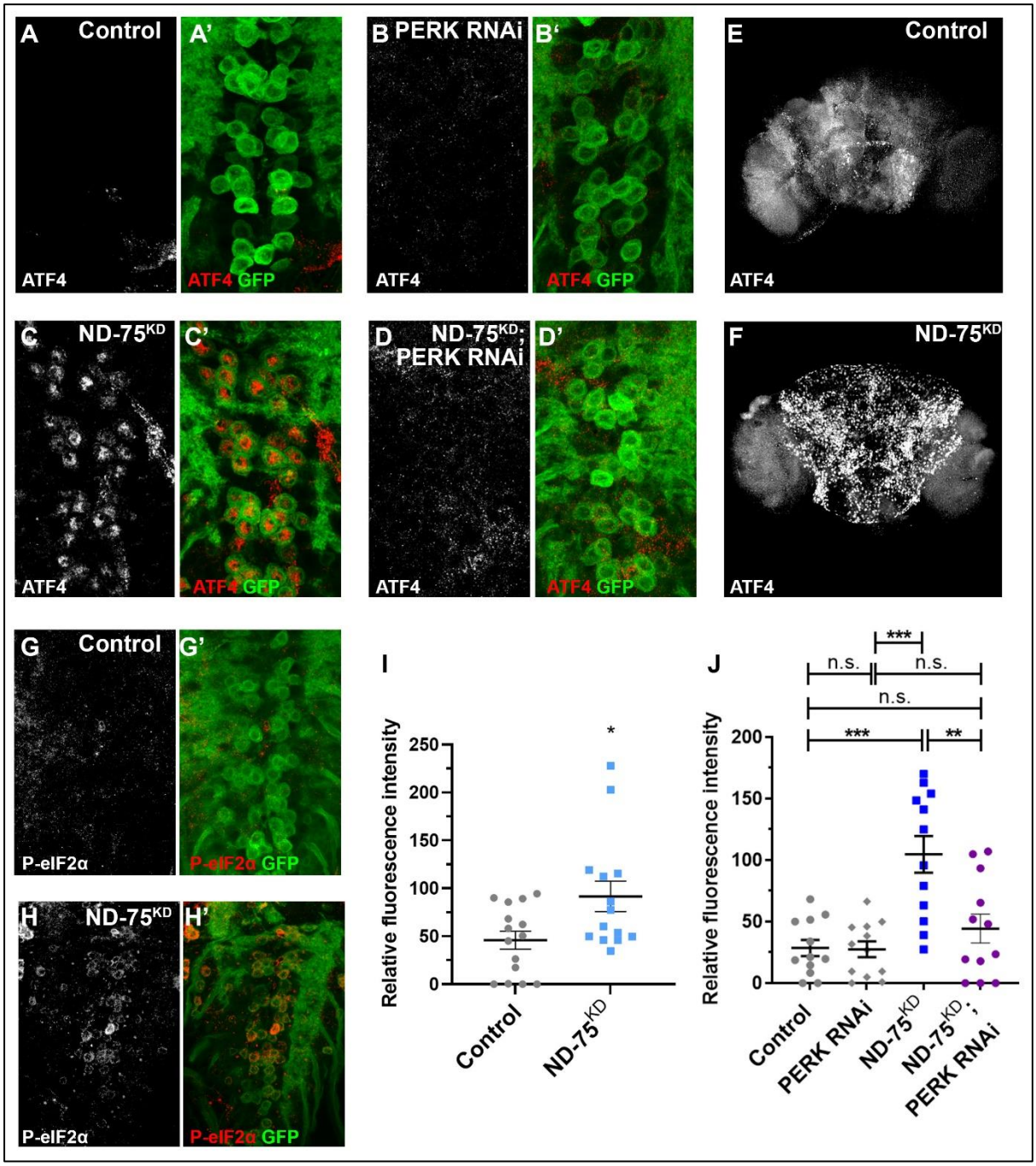

Figure 3. ND-75^{KD} in neurons activates the UPR. (A-D) ATF4 (red) expression in control (A) or ND-75^{KD} (B), PERK knockdown (C), or ND-75^{KD} with PERK knockdown (D) larval motor neurons using *OK371-Gal4*. CD8-GFP (green) expression labels motor neurons. (E, F) ATF4 expression in control (E) or pan-neuronal ND-75^{KD} (F) adult brain tissue using *Tub-Gal80^{ts}*; *nSyb-Gal4*. (G, H) Phospho-eIF2α (P- eIF2α, red) expression in control (G) or ND-75^{KD} (H) larval motor neurons using *OK371-Gal4*. CD8-GFP (green) expression labels motor neurons. (I) Quantification of Phospho-eIF2α expression. Student's t test. (J) Quantification of ATF4 expression. ANOVA with Tukey's posthoc test. Controls are *OK371-Gal4* or *Tub-Gal80^{ts}*; *nSyb-Gal4* hemizygotes. Data are represented as mean ± SEM. n.s. not significant, *p<0.05, **p<0.01, ***p < 0.001.

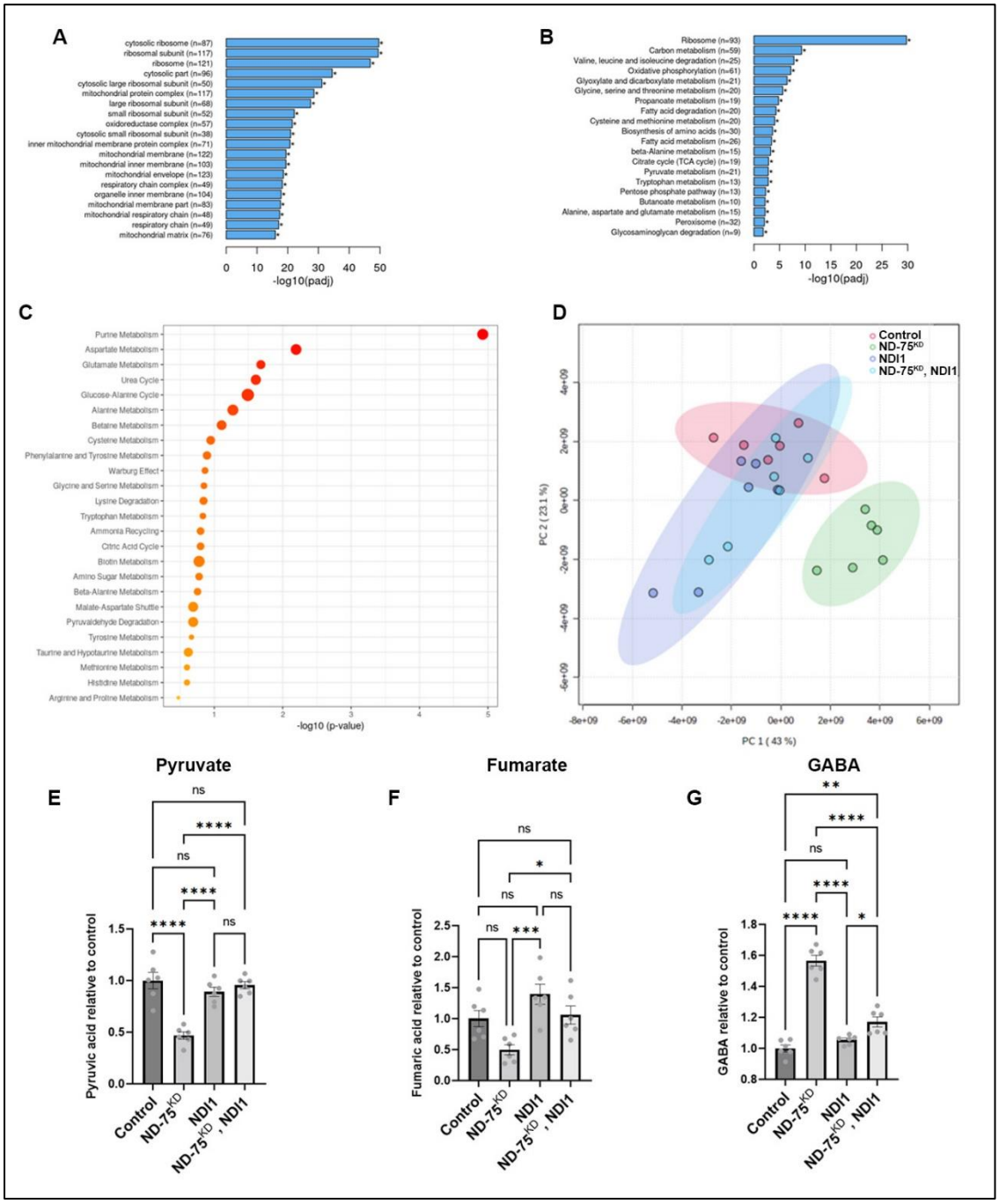

Figure 4. ND-75^{KD} inhibits mitochondrial gene expression and disrupts the TCA cycle in neurons. (A) GEO cellular processes analysis of genes with significantly decreased expression in head tissue from pan-neuronal ND-75^{KD} using *Tub-Gal80^{ts}*; *nSyb*-Gal4. (B) KEGG pathway analysis of genes with significantly decreased expression in head tissue from pan-neuronal ND-75^{KD} using *Tub-Gal80^{ts}*; *nSyb*-Gal4. (C) MSEA analysis of significantly altered metabolites in head tissue from pan-neuronal ND-75^{KD} using *Tub-Gal80^{ts}*; *nSyb*-Gal4. (D) PCA analysis of metabolite levels in head tissue from control, ND-75^{KD}, NDI1 and ND-75^{KD}, NDI1 expressing flies using *Tub-Gal80^{ts}*; *nSyb*-Gal4. (E-G) Levels of pyruvate (E),

fumarate (F) and GABA (G) control, ND-75^{KD}, NDI1 and ND-75^{KD}, NDI1 expressing flies from metabolomic analysis. Controls are *Tub-Gal80^{ts}*; *nSyb-Gal4* hemizygotes. Student's t test. Data are represented as mean ± SEM. ns not significant, *p<0.05, **p<0.01, ***p < 0.001, ***p < 0.0001.

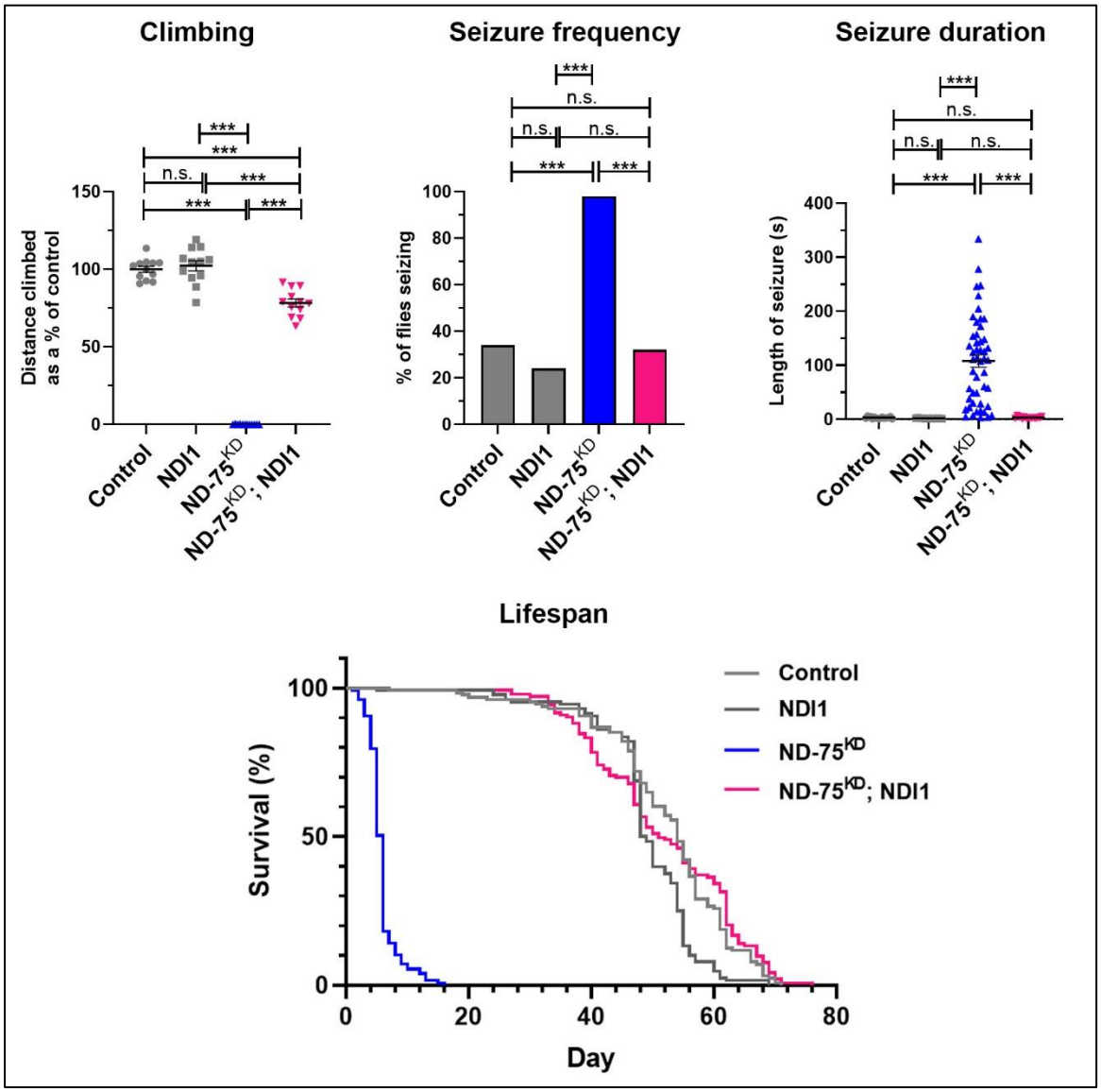

Figure 5. NDI1 expression restores climbing ablility, prevents seizures and early death in ND-75^{KD} flies. (A) Quantification of climbing ability in control flies or with pan-neuronal expression of NDI1, ND-75^{KD}, or ND-75^{KD} with NDI1. (B, C) Quantification of seizure frequency (B) and duration (C) in control flies or with pan-neuronal expression of NDI1, ND-75^{KD}, or ND-75^{KD} with NDI1. (D) Lifespan analysis in control flies or with pan-neuronal

expression of NDI1, ND-75^{KD}, or ND-75^{KD} with NDI1. Lucy add n numbers for lifespan. ND-75 RNAi expressed using *Tub-Gal80^{ts}*; *nSyb-Gal4*. Controls are *Tub-Gal80^{ts}*; *nSyb-Gal4* hemizygotes. Data are represented as mean ± SEM. ANOVA with Tukey's posthoc test, Chi-squared for seizure frequency, or log-rank test for survival curve. n.s not significant, ***p < 0.001.

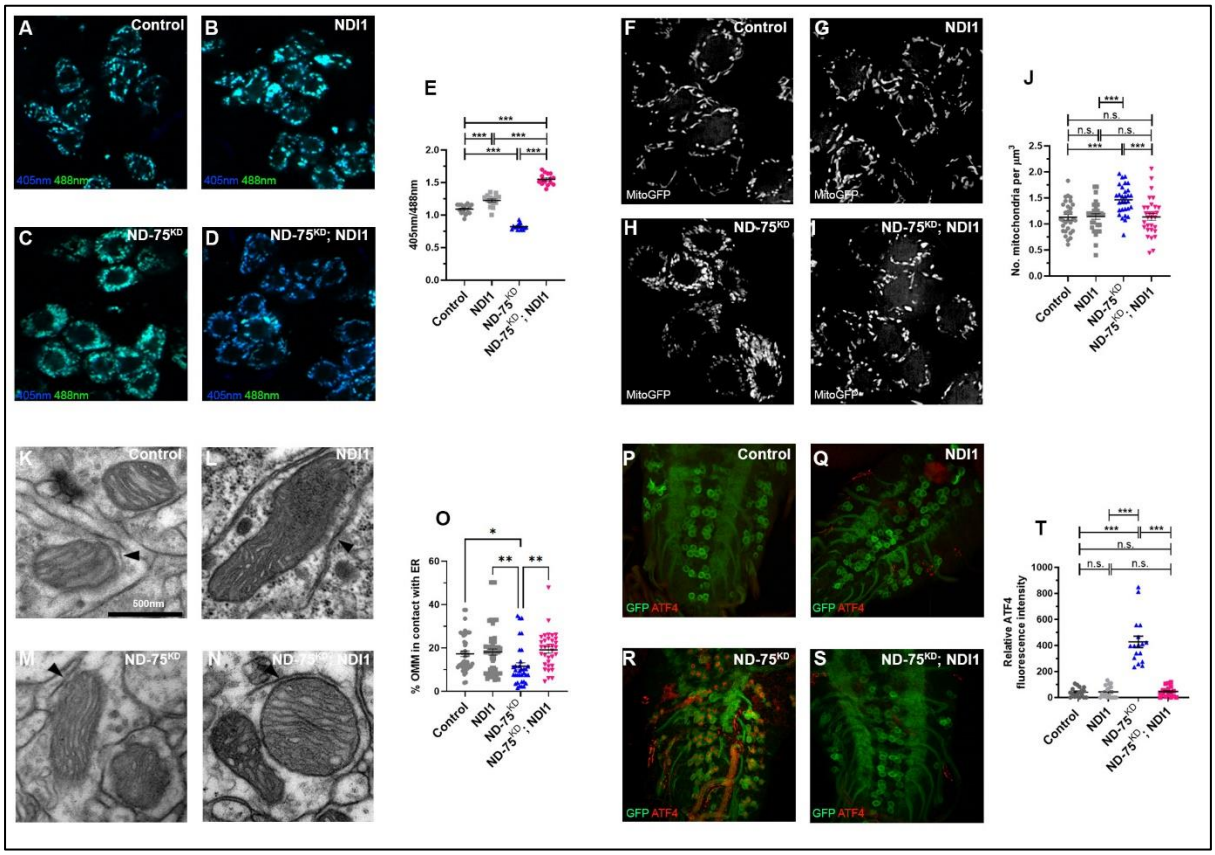

Figure 6. NDI1 expression reverses the mitochondrial defects and prevents UPR activation in ND-75^{KD} neurons. (A-D) mito-roGFP2-Grx1 expression showing merge of 405nm excitation (blue) and 488nm excitation (green) emission fluorescence in control (A), NDI1 expression (B), ND-75^{KD} (C), or ND-75^{KD} with NDI1 (D) larval motor neurons using *OK371-Gal4*. (E) Quantification of mito-roGFP2-Grx1 405nm and 488nm excitation fluorescence. (F-I) Mitochondria-targeted GFP (MitoGFP) expression in control (F), NDI1 expression (G), ND-75^{KD} (H), or ND-75^{KD} with NDI1 (I) larval motor neurons using *OK371-Gal4*. Images taken using iSIM. (J) Quantification of mitochondrial number. (K-N) Transmission electron microscopy images of mitochondria in adult brain tissue from control (K), or pan-neuronal NDI1 expression (L), ND-75^{KD} (M), or ND-75^{KD} with NDI1 (N) using *Tub-Gal80^{ts}*; *nSyb-Gal4*. Arrowheads indicate ER-mitochondria contacts. (O) Quantification of ER-mitochondria contacts. (P-S) ATF4 expression (red) in control (P), NDI1 expression (Q), ND-75^{KD} (R), or ND-75^{KD} with NDI1 (S) larval motor neurons using *OK371-Gal4*. CD8-

GFP expression (green) labels motor neurons. (T) Quantification of ATF4 expression. ANOVA with Tukey's posthoc test. Controls are *OK371-Gal4* or *Tub-Gal80^{ts}*; *nSyb-Gal4* hemizygotes. Data are represented as mean ± SEM. n.s. not significant, *p<0.05, **p<0.01, ***p < 0.001.

Supplemental figures

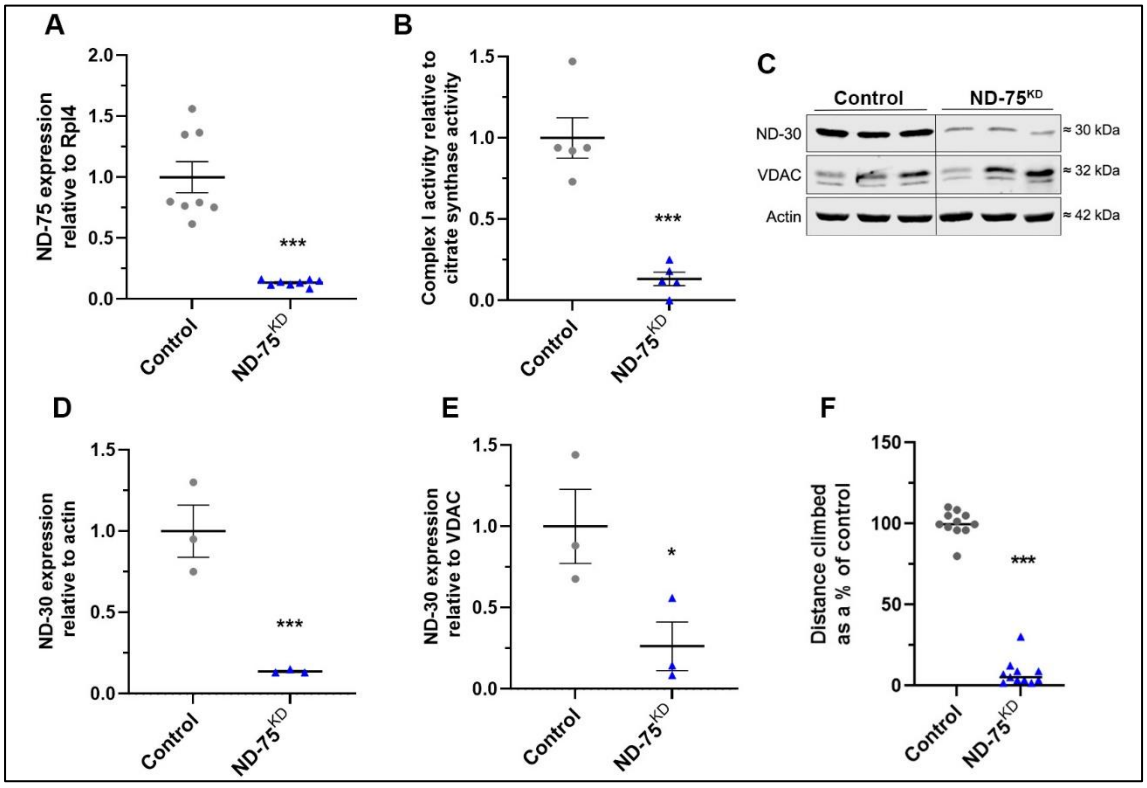

Figure S1. Validation of ND-75^{KD}. (A) qRT-PCR analysis of ND-75 mRNA levels from adult flies with ubiqitious ND-75^{KD} using *Da-GS-Gal4*. (B) Complex I activity in mitochondria isolated from adult flies with ubiqitious ND-75^{KD} using *Da-GS-Gal4.* (C) Western blot analysis of ND-30 expression in adult flies with ubiqitious ND-75^{KD} using *Da-GS-Gal4*. (D, E) Quantification of ND-30 expression relative to actin (D) and the mitochondrial outer membrane protein VDAC (E). (F) Reduced climbing abilty of flies expressing an alternative ND-75 shRNA (HMS00854) in neurons with *Tub-Gal80^{ts}*; *nSyb-Gal4*. Controls are *Da-GS-Gal4* hemizygotes. Student's t test. Data are represented as mean ± SEM. *p<0.05, ***p < 0.001.

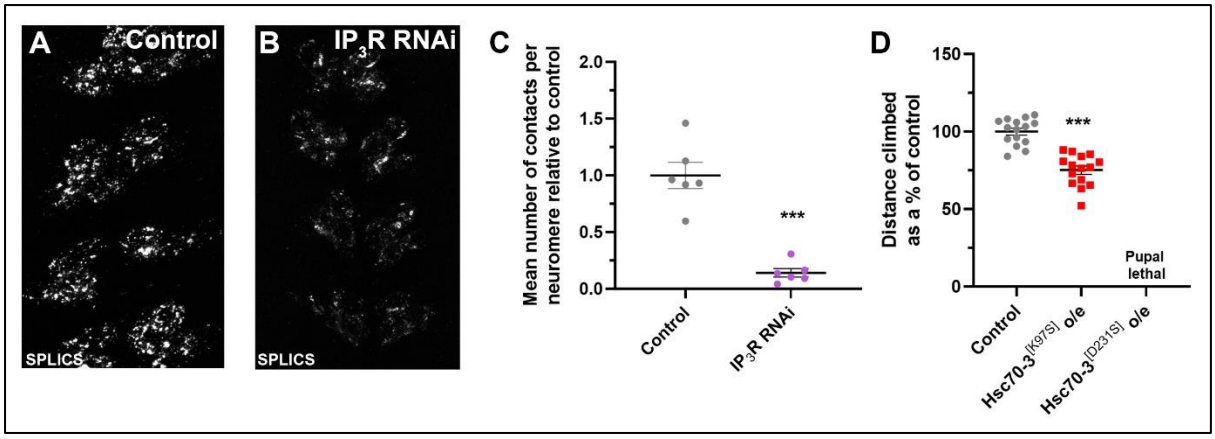

Figure S2. Validation of the SPLICS reporter. (A, B) Visualisation of ER-mitochondria contacts by SPLICS expression in larval motor neurons using *OK371-Gal4* in control (A) and with IP_3R knockdown (B). (C) Quantification of ER-mitochondria contacts. (D) Climbing ability of flies with Hsc70-3$^{[K97S]}$ and Hsc70-3$^{[D231S]}$ overexpression in neurons using *nSyb-Gal4*. Controls are *OK371-Gal4* or *nSyb*-Gal4 hemizygotes. Student's t test. Data are represented as mean ± SEM. ***p < 0.001.

Supplemental tables

Table S1. Genes with significantly decreased expression in head tissue from pan-neuronal ND-75^{KD} using Tub-Gal80^{ts}; nSyb-Gal4. In column N, complex I genes are highlighted in green, complex II genes highlighted in blue (also components of the TCA cycle), complex III genes highlighted in red, compex IV genes highlighted in yellow, complex V genes highlighted in gray. TCA cycle genes are highlighted in orange (except SdhA-D in blue).

Table S2. Genes with significantly decreased expression in head tissue from pan-neuronal ND-75^{KD} using Tub-Gal80^{ts}; nSyb-Gal4.

Table S3. Metabolites with significantly altered levels in head tissue from pan-neuronal ND-75^{KD} using Tub-Gal80^{ts}; nSyb-Gal4.

Table S4. Details of Drosophila strains used.